SCIENCE CHINA
Information Sciences

• RESEARCH PAPER •

February 2026, Vol. 69, Iss. 2, 122302:1–122302:15
https://doi.org/10.1007/s11432-025-4524-6

Reliable contactless microwave cardiogram detection with interferometric biomedical radar

Shuqin DONG[1], Li WEN[1], Qing CAO[2], Kang CHEN[2], Changzhan GU[1*] & Junfa MAO[1]

[1]*State Key Lab of Radio Frequency Heterogeneous Integration, Shanghai Jiao Tong University, Shanghai 200240, China*
[2]*Ruijin Hospital, Shanghai Jiao Tong University School of Medicine, Shanghai 200025, China*

Received 13 January 2025/Revised 20 May 2025/Accepted 22 July 2025/Published online 4 January 2026

Abstract Radar-based contactless detection of detailed cardiac activity enables convenient and accurate heart monitoring in healthcare applications. However, it requires further investigation regarding the reproducibility of stable characteristic cardiogram waveforms. In this study, we initially perform a systematic link-budget analysis for radar-based cardiogram detection to derive the performance requirements for the radar system to be used in the detection of weak cardiogram signals. Then, we propose a novel velocity cardiogram (VCG) extraction framework, which employs vector analytic demodulation (VAD)-Wiener filtering, to accurately extract cardiograms based on the signals obtained using an interferometric biomedical radar. The obtained VCG waveforms provide more stable cardiogram waveforms than Doppler cardiogram waveforms in terms of reproducibility. We conducted clinical experiments to obtain cardiac activity data from individuals with various body types and ages, covering 6123 cardiac cycles in total. The results showed that the proposed framework provides stable velocity cardiogram waveforms, which can be used to extract physiologically meaningful characteristics. In addition, the extracted RR intervals from all detected cardiac activities show a correlation of 0.987 with the ground-truth ECG, validating the high stability and reliability of the proposed cardiogram detection framework.

Keywords Doppler cardiogram, morphology analysis, heart monitor, remote detection, velocity cardiogram

Citation Dong S Q, Wen L, Cao Q, et al. Reliable contactless microwave cardiogram detection with interferometric biomedical radar. Sci China Inf Sci, 2026, 69(2): 122302, https://doi.org/10.1007/s11432-025-4524-6

1 Introduction

The detection of cardiac activity is crucial for the diagnosis and management of various heart-related diseases. Traditional methods, such as electrocardiography (ECG) [1], ballistocardiography (BCG) [2], and seismocardiography (SCG) [3, 4] have been widely used; however, they often require probes in direct contact with the human body, making them impractical in clinical environments. The continuous progress in radar technology has provided continuous-wave interferometric radars with excellent capabilities of detecting target micromotions [5]. Recently, radar-based cardiogram detection methods, such as the Doppler cardiogram (DCG) method [6], have emerged as promising contactless techniques for the continuous and unobtrusive monitoring of heart activity. Understanding the relationship between radar-based and traditional cardiograms is essential for obtaining insights into the different aspects of cardiac activity. For example, ECG detects the electrical depolarization and repolarization cycles within the heart, and DCG provides insights into the resultant mechanical motions, such as the combined movement of atria and ventricles. As a result, a combined view of cardiac health can be obtained. This dual perspective is essential for comprehensive cardiac assessments, particularly in cases where the electrical patterns cannot fully reveal mechanical dysfunctions such as heart valve diseases or aortic dissections [7].

However, large-scale studies on radar-based cardiogram reproducibility have not been conducted. Therefore, there is a lack of knowledge on the stability of radar-based cardiogram waveforms across different populations and the distortions in the radar-based cardiogram waveforms induced by various radar-detection methods.

Based on the characteristics of quadrature radar signals, several high-linearity demodulation algorithms have been proposed to accurately recover phase information in radar interferometry and obtain time-domain waveforms of the target motion. These algorithms include arctan [8], DACM [9], arcsine [10], and MDACM [11]. All these algorithms are used to linearly and accurately reconstruct the waveforms corresponding to target displacement. In some previous studies, machine- or deep-learning techniques were used to detect cardiograms; this requires the precollection of radar and gold-standard ECG data. Then, the model is trained to transform radar-detection signals

* Corresponding author (email: changzhan@sjtu.edu.cn)

into quasi-ECG waveforms [12, 13]. Although this method exploits the advantages of deep-learning models, it lacks interpretability. The detected cardiograms do not correspond true physiological signal, making it difficult to validate the authenticity of their waveform morphology.

The chestwall displacement signal obtained after radar signal demodulation is a mixed signal of respiratory and heartbeat activities. The linear and distortion-free extraction of the human cardiogram, and as well as the calculation of specific cardiac activity intervals based on characteristic waveforms, are currently hot research topics. In recently published articles, a parameter respiratory filter (PRF) [7] was used to accurately filter out respiratory motions to extract cardiogram waveforms. Additionally, other methods based on wavelet transforms [14, 15] and empirical mode decomposition [16, 17] have been used to extract heartbeat waveforms. However, these algorithms face challenges in practical applications because of the difficulty of adaptively the randomness of physiological signals.

In addition to the detection of cardiac activity waveforms, radar-based cardiograms can provide accurate cardiac interval parameters, such as RR and RT intervals, because of the strong coupling characteristics between radar-based cardiograms and ECG. A DCG-RT-detector method [18] has been proposed to directly detect the positions of characteristic waveforms in DCG to obtain the RR intervals. Additionally, some studies have exploited the biological nature of the coupling between cardiac electrical activity and mechanical activity [12, 19]. In these studies, radar cardiac cycles and ECG signals were simultaneously acquired, and deep learning, as well as synchronized data training, was employed to reconstruct the ECG waveforms based on the obtained radar signals. This approach enables the identification of important characteristics, such as QRS waves, enabling the calculation of time-domain parameters such as RR intervals.

In this study, our objective is to achieve distortion-free acquisition of cardiograms and investigate their waveform repeatability and robustness across diverse populations. Based on their generation mechanism, radar-based cardiograms contain rich waveform details that reflect the activities of the heart and its four chambers [6]. Given the quasi-stationary yet nonstationary nature of human vital signals, the linear adaptive extraction of cardiogram waveforms is crucial.

In this study, we propose a framework to accurately extract highly reliable cardiac activity. The key contributions of our work are summarized as follows.

- The velocity cardiogram (VCG) and its related physiological model are proposed, and the radar link analysis of the VCG detection is performed, providing a theoretical basis.
- A novel linear cardiogram extraction algorithm with adaptive waveform characteristics is proposed, which offers high accuracy and linearity in VCG recovery.
- Validation of the v- and n-wave waveforms of the proposed VCG across a wide range of ages and body weights by obtaining 6123 heart cycles in total. Our results verify that the extracted VCG waveforms show outstanding stability compared to DCG in terms of waveform consistency.
- Validation and discussion of the VCG detection results under different scenarios. Our results show that different radar-based detection scenarios can lead to waveform distortions in the VCGs. Specifically, when a radar irradiates different areas of the human body, the resulting VCG waveforms may vary in shape.

Considering population universality, in this study, we extensively analyze human VCGs and define their characteristic waveforms. The extracted v- and n-wave waveforms correspond to the maximum-velocity points of different motion trends in cardiac mechanical activity. Our analysis and results enable further applications of radar systems in cardiac activity detection, thus contributing to the establishment of large datasets that support AI applications.

2 Theory

2.1 Radar cardiogram mechanism

Radar cardiogram, as an emerging technology, is susceptible to signal quality variations caused by individual differences (e.g., body fat percentage, thoracic cavity structure, skin impedance) and environmental interference (e.g., distance, motion artifacts). Current research predominantly investigates the biomedical significance of remotely detected cardiac activity signals via radar and focuses on optimizing signal acquisition algorithms, yet lacks systematic validation of waveform consistency across diverse populations. Functional descriptors of cardiac activity, such as electrocardiograms (ECG) exhibit well-defined characteristic waveforms with similar morphological patterns across populations, as shown in the display of ECG device in Figure 1.

The proposed VCG in this work characterizes mechanical cardiac velocity signals, whereas prior DCG methodologies quantified volumetric cardiac changes [6]. Cardiac volumetric changes primarily originate from chamber

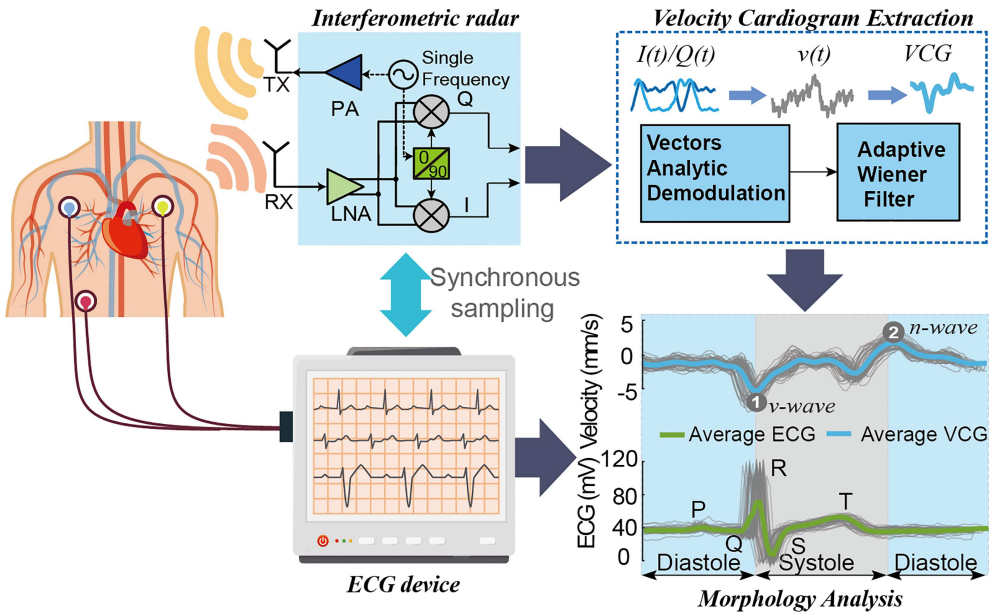

Figure 1 (Color online) Detailed block diagram of the proposed remote velocity cardiogram detection framework with interferometric biomedical radar.

contraction/relaxation dynamics, reflecting cardiac preload (filling pressure) and afterload (arterial resistance). In contrast, cardiac velocity metrics (e.g., myocardial contraction velocity, blood flow velocity) reflect instantaneous biomechanical performance of myocardial fibers, exhibiting lower sensitivity to preload/afterload fluctuations. Volumetric metrics are prone to low-frequency perturbations induced by loading conditions, whereas velocity metrics predominantly depend on intrinsic myocardial contractility [20].

Volumetric indices face limitations in early pathological states. For instance, ventricular dilation may compensate for reduced stroke volume in early heart failure, whereas myocardial contraction velocity abnormalities manifest earlier in ischemia or fibrosis with minimal compensatory interference. Thus, velocity metrics demonstrate superior stability in pathological conditions [21]. Comparative analyses of VCG and DCG waveform stability under pathological states will be presented in responses to your second and third queries. Low-frequency disturbances (e.g., respiration, postural changes) significantly affect volumetric measurements. Velocity signals (e.g., Doppler flow) inherently represent differentials of volumetric signals, amplifying high-frequency transient features (e.g., peaks, edges) while suppressing low-frequency baseline drift. This differential nature enhances waveform stationarity.

2.2 Link budget analysis

For the heart motion detection scenario, as shown in Figure 2, first, we need to calculate the radar received power of the signal reflected by the effective chest area. In the scenario of single-transmitter single-receiver 24 G continuous wave radar vital signs detection, the radar's equivalent detection target is the entire chest cavity, and the beam is focused on the whole chest not only the heart area. Therefore, the effective echo reflection carrying the vital signs signal should come from the entire chest wall. The received power P_r in our continuous-wave (CW) radar system is derived from the radar equation:

$$P_r = \frac{P_t G_t G_r \lambda^2 \sigma_{\text{eff}} L_{\text{body}}}{(4\pi)^3 R^4 L_{\text{path}}}, \tag{1}$$

where P_t is radar transmit power, G_t is transmit antenna gain, G_r is receiving antenna gain, λ is wavelength, σ_{eff} is effective radar cross-section (RCS) of human chest wall, R is target distance, L_{path} is free-space path loss, L_{body} is tissue reflection loss. It is worth noting that, since the detection scene of the bioradar system is often short-range, the free-space path loss L_{path} can be ignored and since the human body is a conductive medium, there is reflection loss on the skin surface.

The radar system used in this article is a mono-static radar, the transmitting and receiving antennas are designed in the same way, the operating frequency is 24 G, the working mode is CW, and P_t is 0 dBm (measured result). So, $G_t = G_r$ =13 dBi, and the wavelength λ is 1.25 cm, target distance R is 50 cm, antenna size is 3 cm × 2 cm, target lies in far-field condition.

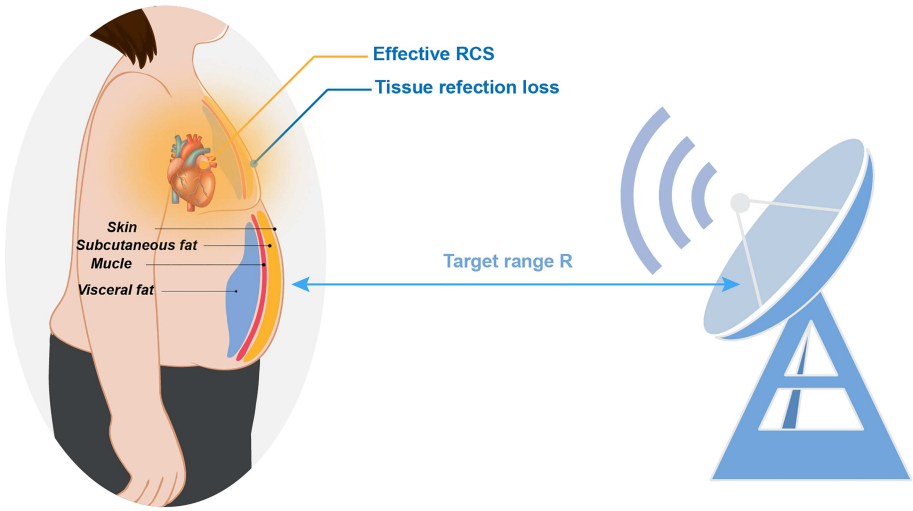

Figure 2 (Color online) Schematic diagram of the application of the radar equation in vital sign detection.

According to the catalog and technical requirements for low-power short-range radio transmitting equipment issued by the Ministry of Industry and Information Technology of the People's Republic of China, the equivalent isotropic radiated power (EIRP) of equipment in 24 GHz frequency band cannot exceed 20 mW. For the bio-radar system in this article, EIRP $= P_t^* G_t = 20$ mW, which meets the safety standard.

The RCS corresponding to human cardio-respiratory motion is measured in [22]. Based on the relationship between wavelength and RCS, the effective σ_{eff} of cardiopulmonary motion area at 24 GHz is 1.2 m^2.

At a frequency of 24 GHz, the loss of electromagnetic waves when reflected by the human body surface is mainly determined by the reflection coefficient. According to the electromagnetic parameters, the conductivity of human dry skin obtained in $\sigma = 22.84$ S/m, relative permittivity $\varepsilon_r = 18.993$ [23]. The intrinsic impedance of human tissue η_{body} can be calculated

$$\eta_{\text{body}} = \frac{\eta_0}{\sqrt{\varepsilon_r - \text{j}\frac{\sigma}{w\varepsilon_0}}} = 18.944 + \text{j}4.124, \tag{2}$$

where $\eta_0 = 377$ is free-space wave impedance, $w = 2 \times 24 \times 10^9$ rad/s, $\varepsilon_0 = 8.854 \times 10^{-12}$ F/m. Therefore, the reflection coefficient at normal incidence is

$$\Gamma = \frac{\eta_{\text{body}} - \eta_0}{\eta_{\text{body}} + \eta_0} \approx -0.9 + \text{j}0.0198. \tag{3}$$

Tissue reflection loss $L_{\text{body}} = |\Gamma|^2 \approx 0.81$, finally the calculated received power $P_r = -31.13$ dBm.

Then, we need to analyze the noise source and estimate the signal-to-noise ratio of the radar receiver. In the zero-IF Doppler radar system for short-range sensing discussed in this paper, residual phase noise is negligible, with the primary noise contributions being baseband $1/f$ noise and additive Gaussian noise. First, it is necessary to calculate the noise floor N_0 of the receiver system primarily composed of Johnson-Nyquist thermal noise. The noise floor is determined as

$$N_0 \text{ (dBm)} = kTB + \text{NF} = -158 \text{ (dBm)} + 5 \text{ (dB)} = -153 \text{ dBm}, \tag{4}$$

where k represents Boltzmann's constant, T denotes absolute temperature, B indicates system bandwidth (with ADC sampling rate of 100 Hz and final digital signal bandwidth of 50 Hz in this implementation), and NF corresponds to the noise figure of the receiver's low-noise amplifier (LNA024_005@Silicon with NF = 5 dB in this design).

However, according to flicker noise analysis in [24–26], the flicker noise power in zero-IF systems can exhibit approximately 10–30 dB elevation over the noise floor within the 0–1 Hz bandwidth. Therefore, to rigorously assess the receiver noise performance of the radar, we take the radar receiver's noise floor within 0–1 Hz as

$$N_{0\text{–}1} \text{ (dBm)} = N_0 + 30 \text{ (dB)} = -123 \text{ dBm}. \tag{5}$$

For human targets in a resting state, the effective motion information detected by CW radar is mainly the superposition of the chest surface displacement caused by respiratory movement and heartbeat movement. The amplitude of respiratory movement is generally about 10 times the amplitude of heartbeat movement [26]. Cardiogram

detection requires rich cardiac waveform detail detection capabilities. The amplitude of these fine-grained waveform details is about one-fiftieth of the heart motion amplitude [6]. Therefore, the SNR requirement for detecting cardiograms needs to be 54 dB higher than that for detecting respiratory movement. The SNR requirement for the original baseband signal of effective CW radar IQ channels linear demodulation is 30 dB [11, 18]. Considering these two SNR requirements, we can conclude that the $\mathrm{SNR}_{\mathrm{demand}}$ required for detecting cardiac activity signals is 84 dB.

Then, according to the above analysis, for the proposed radar system detection method in this paper, $P_r - N_{0-1} = 90.87$ dB $> \mathrm{SNR}_{\mathrm{demand}}$. So, it effectively detects the details of heart activity.

In summary, according to this analysis, we can see that for the 24 G CW radar system, the higher the radar transmission power, the greater the antenna gain, the better the noise coefficient performance of the receiver, and the closer the target detection distance (not less than the far-field detection condition), the better the detection performance of heart movement.

2.3 Detection distance analysis

The energy of the human body's backscattered signal received by the radar receiver is inversely proportional to the fourth power of the distance R between the human body and the radar. Therefore, the closer the human body is to the radar, the stronger the backscattered signal energy, and consequently, the better the SNR performance of the radar receiver. For CW radar, static clutter can be eliminated regardless of the target distance.

However, there are two limitations that prevent the target from being too close to the radar. First, our linear target detection theory is derived under the condition of far-field detection by the antenna. Therefore, the target distance should satisfy the far-field detection condition, i.e., $R > 2D^2/\lambda = 25.6$ cm (where D is the antenna diameter).

Second, the backscattered signal energy must not exceed the dynamic range of the radar receiver (which is often determined by the 1 dB compression point of the LNA, due to its nonlinear distortion). Otherwise, the received signal will be distorted. The LNA_024@Silicon used in this paper has a $P_{1\ \mathrm{dB}} = 6.5$ dBm. Based on the calculation of received power P_r in the previous subsection, when received power $P_r = -6.5$ dBm, the calculated closest detection distance is 13.58 cm.

As for the maximum detection limitation, according to the radar equation (1), if the target is too far away, the received backscattered energy will be too small. Therefore, the farthest detection distance for the human body target in the cardiogram detection scenario can be estimated based on the required SNR for receiving the cardiac waveform signal. According to the above analysis, to effectively detect the cardiogram signal, $P_r - N_{0-1}$ needs to be larger than $\mathrm{SNR}_{\mathrm{demand}}$. Finally, the farthest detection distance for the target using the radar system in this paper is calculated as 89 cm.

Since real world radar detection scenarios are more complex and variable, this section has only analyzed the main factors affecting detection. Thus, the optimal detection range of the radar system used in this paper is probably between 15 and 85 cm.

3 Methodology

3.1 Signal model

In the past, the general principle of radar vital sign detection was to explore the thoracic displacement information contained in the phase of the electromagnetic waves reflected from the human body [6]. So, the analysis of radar echo signals often attempts to demodulate the target displacement $x(t)$ from the echo phase, as shown in the following equation:

$$s_R(t) = A_r \cdot \sin\left(\theta_{\mathrm{CW},R} + \frac{4\pi x(t)}{\lambda} + \varphi_0\right), \tag{6}$$

where A_r is the amplitude of echo signal, λ is the wavelength, $\theta_{\mathrm{CW},R}$ is the phase delay caused by R_0, φ_0 is the residual phase.

Under resting conditions, the vibrations on the human thorax, $x(t)$, primarily consist of respiratory movements $x_r(t)$, heart movement $x_h(t)$ and random body movement $x_b(t)$ [27]. These movements are directly superimposed, thus resulting in

$$x(t) = x_r(t) + x_h(t) + x_b(t). \tag{7}$$

The random body movement signal is generally considered to be a relatively stable trend based on experience, and therefore can be regarded as a constant over a short period of time. In this morphology study of the radar cardiogram, we aim to directly obtain the velocity information of thoracic micro-movements. Therefore, we re-model the radar echoes under the cardiogram detection scenario, the echo signal $S_R(t)$ can be expressed as

$$\begin{aligned} S_R(t) &= A_r \cdot \sin\left(2\pi f_t \left(t - T_R\right)\right) \\ &= A_r \cdot \sin\left(2\pi f_t \left(t - 2\frac{R_0 - vt}{c}\right)\right) \\ &= A_r \cdot \sin\left(2\pi f_t \left(\frac{2vt}{c} + 1\right) t - \frac{4\pi R_0 f_t}{c}\right), \end{aligned} \tag{8}$$

where c is the speed of light, R_0 is the initial distance between human and radar, v is the radial instantaneous velocity of the chest-wall under test relative to the radar at time t, and f_t is the operation frequency of radar.

After the downconverter process, the detected in-phase (I) and quadrature-phase (Q) signals scattered by the skin can be obtained

$$I(t) = A_I \cdot \cos\left[\frac{4\pi vt}{\lambda} + \frac{4\pi R_0}{\lambda} + \varphi_0\right] + \mathrm{DC}_I(t), \tag{9}$$

$$Q(t) = A_Q \cdot \sin\left[\frac{4\pi vt}{\lambda} + \frac{4\pi R_0}{\lambda} + \varphi_0\right] + \mathrm{DC}_Q(t), \tag{10}$$

where A_I and A_Q are the amplitudes of the signals, respectively, $\mathrm{DC}_I(t)$ and $\mathrm{DC}_Q(t)$ are the DC offsets.

3.2 Linear signal demodulation

For a normal IQ balanced radar system, based on the principle of vectors analytic demodulation (VAD) algorithm proposed in previous work [18], the discrete velocity of chest-wall movement $v(nT)$ in discrete with a signal length L and sampling interval T can be written as

$$\begin{bmatrix} v(0) \\ \vdots \\ v(iT) \end{bmatrix} = \frac{\lambda}{4\pi A^2} \cdot \begin{bmatrix} I(0)\cdot\hat{Q}(0) & \hat{I}(0)\cdot Q(0) & \hat{Q}(0) & \hat{I}(0) \\ \vdots & \vdots & \vdots & \vdots \\ I(iT)\cdot\hat{Q}(iT) & \hat{I}(iT)\cdot Q(iT) & \hat{Q}(iT) & \hat{I}(iT) \end{bmatrix} \cdot \begin{bmatrix} 1 \\ -1 \\ -\mathrm{DC}_I \\ \mathrm{DC}_Q \end{bmatrix}, i \in [0, L], \tag{11}$$

where i represents the ith sampling point of the processed digital signal.

It can be seen that the velocity of chest-wall movement signal $v(t)$ shares a linear relationship with four vectors: $\hat{I}(t)$, $\hat{Q}(t)$, $I(t)\cdot\hat{Q}(t)$ and $Q(t)\cdot\hat{I}(t)$.

In DCG morphology analysis, the focus is on the temporal waveform patterns of the demodulated signal, not its absolute displacement. Therefore, according to (6), we can linearly demodulate the velocity signal of the thorax.

3.3 Cardiogram extraction

Eq. (2) illustrates the components of thoracic movement. Over a shorter period of time, the thoracic movement velocity v has the following relationship with the thoracic movement velocity $v_h(t)$ caused by the heart and the thoracic movement velocity $v_r(t)$ caused by respiration:

$$v(t) = v_r(t) + v_h(t). \tag{12}$$

In past related research, many studies have modeled heartbeat and respiratory signals as ideal mathematical models. Based on these data models, the characteristics of physiological signals are accurately estimated to extract heartbeat or respiratory movements [7]. However, in practical situations, physiological signals are stochastic, and the breathing and heart rates of the human body are not constant.

In physiology, respiration involves inhalation and exhalation phases [28]. During inhalation, the diaphragm contracts and flattens, pushing the abdominal cavity downward. The expansion of the thoracic and abdominal cavities increases lung volume and decreases thoracic pressure. Exhalation relaxes the diaphragm, allowing the thoracic and abdominal cavities to return to their resting state. Also, the volume changes of the heart resulting from its pumping action reflect the periodic nature of the cardiac cycle, where the heart undergoes regular contractions (systole) and relaxations (diastole) to pump blood throughout the body. Over each cardiac cycle, the heart's volume oscillates

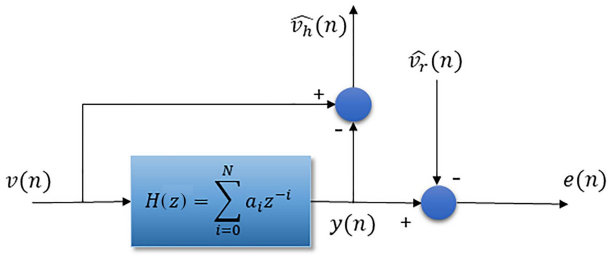

Figure 3 (Color online) Block diagram of proposed optimal FIR Wiener filter.

between its maximum (end-diastolic volume) and minimum (end-systolic volume) values in a predictable and repetitive manner. Under resting state, the heart volume change and respiratory movement maintain consistent amplitude and frequency characteristics, indicating stable cardiac function, which is crucial for maintaining consistent blood flow and pressure, ensuring efficient circulation and oxygen delivery to tissues. Therefore, physiological signals can be modeled as stationary random processes over short periods.

In the process of analyzing cardiogram waveforms, we aim to develop a new adaptive filter for processing stationary random signals to extract the VCG $v_h(t)$ from $v(t)$ without distortion. In this work, a linear optimal discrete filter, the finite impulse response (FIR) Wiener filter method is proposed. Figure 3 establishes the signal block diagram for the proposed filter method. The input event sequence of the filter is the demodulated thoracic motion velocity signal $v(0)$, $v(1)$, ... and the filter is characterized by the transfer function $H(z)$:

$$H(z) = \sum_{i=0}^{N} a_i z^{-i}, \tag{13}$$

where N is the order of the FIR Wiener filter. It should be noted that our choice of the FIR filter here is primarily based on practical application scenarios. The FIR filter structure utilizes only the forward path without feedback, which inherently ensures stability. This inherent stability is necessary for the adaptive filter optimization process in this work.

During the process of cardiogram extraction, we regard the respiratory signal $v_r(t)$ as noise. However, based on empirical information about human vital signs, respiratory waveforms generally exhibit a stable frequency distribution (0–0.6 Hz) over short periods, while cardiac activity waveforms are more complex. Therefore, in the design process of the optimal linear Wiener filter, we assume that the original thoracic velocity discrete signal $v(n)$, when processed through the aforementioned optimal FIR Wiener filter, yields $y(n)$ that approximates the respiratory activity velocity signal $v_r(n)$ as closely as possible. In the optimization process of the optimal Wiener filter, we pass the demodulated original thoracic motion velocity signal $v(n)$ through an FIR low-pass filter $g(n)$ with a cutoff frequency of 0.6 Hz to generate a respiratory estimation signal $\widehat{v}_r(n)$:

$$\widehat{v}_r(n) = \sum_{m=0}^{N-1} g(m)v(n-m), \tag{14}$$

where N is the number of samples of $v(n)$. Then, the optimal process for the FIR Wiener filter is achieved by calculating the filter coefficients $H(z)$ that minimize the mean square error $e(n)$:

$$e(n) = E\left\{[y(n) - \widehat{v}_r(n)]^2\right\}. \tag{15}$$

Finally, based on the superposition principle of the linear Wiener filter, the optimal estimation signal of the VCG, denoted as $\widehat{v}_r(n)$, can be obtained as

$$\hat{v}_r(n) = v(n) - y(n). \tag{16}$$

By applying the optimal FIR Wiener filter, we can effectively separate the cardiogram signal from the breathing interference, providing a cleaner and more accurate representation of the cardiogram signal.

3.4 Segmentation of VCG waveform

The segmentation of cardiac activity cycles is fundamental for studying the reproducibility of VCG waveforms. According to the physiology of cardiac mechanical activity, during ventricular contraction, rapid blood pumping

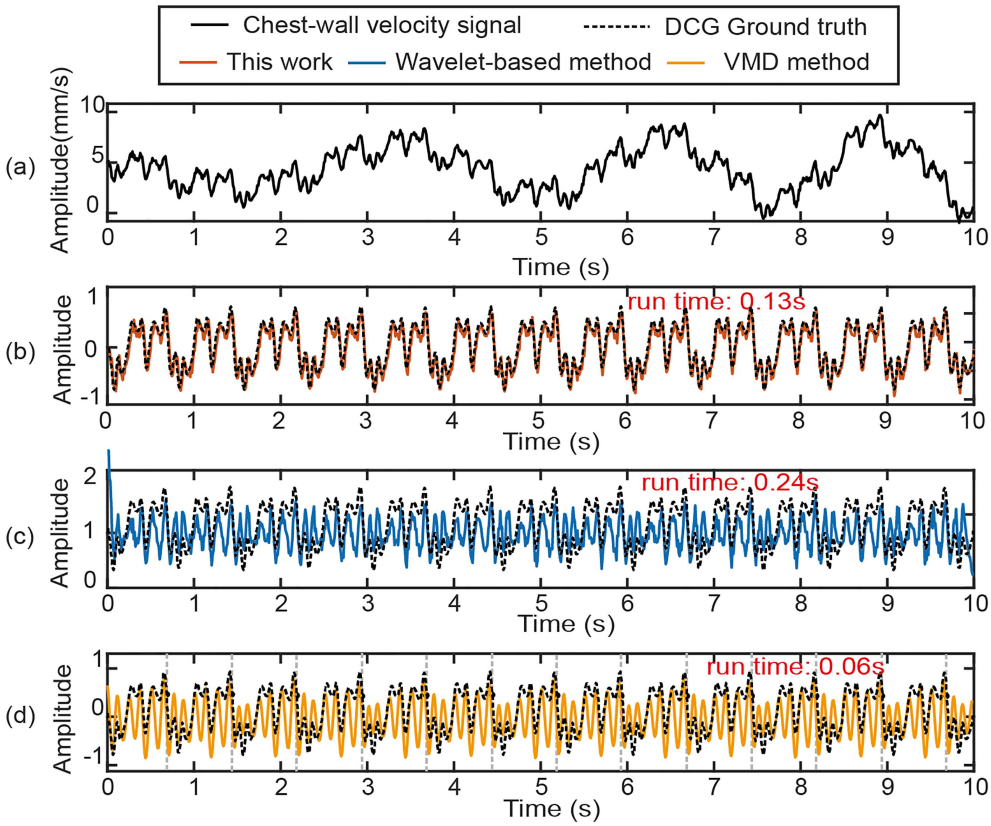

Figure 4 (Color online) (a) Simulated chest-wall velocity signal; (b)–(d) the demodulated results of different algorithms. The grey dotted line in (d) identifies the QRS characteristic waveform.

generates high velocity values, resulting in sharp peaks in the VCG. This characteristic of the waveform is particularly advantageous for calculating and segmenting the cardiac intervals of the VCG waveform.

To enhance this characteristic of the waveform and achieve a precise segmentation of cardiac activity, we applied a cubic transformation to the extracted VCG signals $v_h(t)$. This approach effectively amplifies peak signals and suppresses low-amplitude and flat signals, as follows:

$$\text{Peaks}\ (n) = [v_h(n)]^3 . \tag{17}$$

Subsequently, we use a peak detection algorithm to achieve the segmentation of cardiac activity cycles.

4 Experiments and results

4.1 Simulation

To verify the performance advantages of the proposed algorithm in this paper for processing stationary random signals, we conducted signal simulations using MATLAB. During the simulation process, we used the DCG waveform derived from the cardiac MRI data presented in [6] as the heart activity signal. For the respiratory signal, we used the respiratory model proposed in [7]. To reflect the randomness of the signal, we allowed the respiratory rate f_b to fluctuate slightly over the simulation time. It should be noted that in this scenario, the respiratory rate is variable; therefore, some algorithms that rely on accurate respiratory rate estimation to remove respiratory waveforms for cardiogram extraction, such as the PRF algorithm, are no longer applicable.

Figure 4 presents the simulation results for a 10-s time window. Figure 4(a) shows the thoracic motion velocity signal after radar baseband demodulation. Figures 4(b)–(d) show the results of different signal extraction algorithms, along with their respective running times. Figure 4(b) shows the results of the adaptive Wiener filter algorithm proposed in this work, which almost perfectly matches the true signal. In contrast, the waveforms extracted by the empirical wavelet transform shown in Figure 4(c) and the variational mode decomposition shown in Figure 4(d) differ significantly from the true values. By comparing the waveform processing results of the proposed Wiener filter

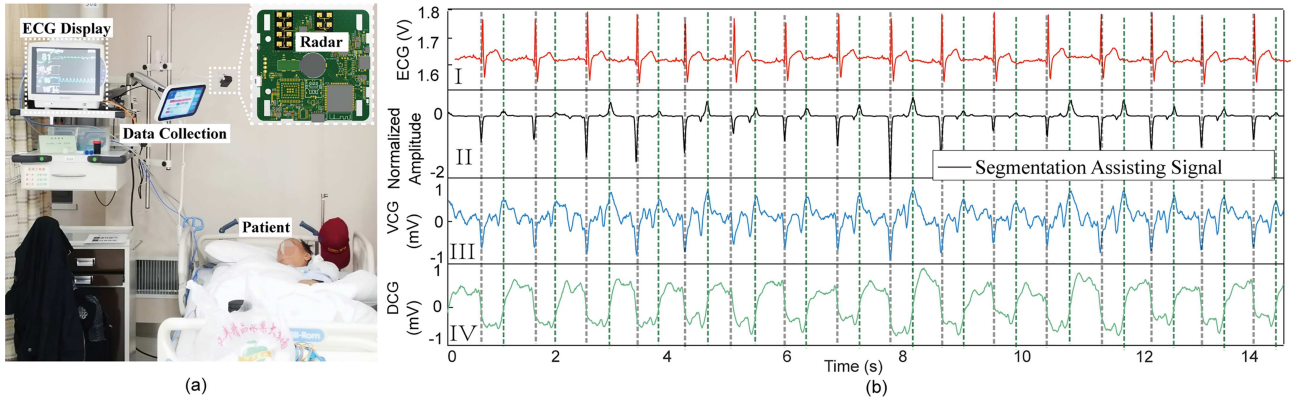

Figure 5 (Color online) (a) The clinical experiment setup. Insert is the picture of custom-designed radar system. (b) Comparison between the extracted DCG, VCG, segmentation assisting signal and the ECG signals.

method with those of the existing algorithms, it is evident that the Wiener filter method demonstrates superior waveform recovery performance. This discrepancy may be attributed to the fact that, as shown in Figure 3, the proposed Wiener filter method incorporates an adaptive negative feedback mechanism. This feature makes it more suitable for processing VCG signals, which are approximately stationary but do not maintain a perfectly consistent period.

4.2 Experimental setup

Figure 5(a) illustrates the experimental setup. The experiment was conducted in a clinical environment, as depicted in the figure. The subject was positioned supine on a bed, with their chest facing upward. The radar sensor was mounted on a fixed structure, approximately 50 cm above the subject's chest. During the measurement, the subject breathed normally. The temperature of the inpatient ward was maintained at 26°C. Based on our analysis of the application scenario, a convenient installation position for the radar in a sleeping posture scenario is at a vertical height of 40 cm to 1 m from the human body, located at the head of the bed. This position does not interfere with daily activities such as getting into bed. It is noted that the detection distance in this paper has taken into account the linear detection range of the radar system, the required SNR for acquiring cardiac waveform signals, and the actual needs of the application scenario.

The inset of Figure 5(a) shows the implementation of the Doppler radar sensor, which is based on a 24-GHz front-end silicon-germanium millimeter-wave integrated circuit (MMIC@SGR). Additionally, a K-band low noise amplifier (LNA@Silicon radar) is employed to enhance the noise figure performance of the receiver. The baseband signals are sampled by the built-in 16-bit sigma-delta analog-to-digital converters (ADCs) in the microcontroller unit (MCU). The designed radar sensor, measuring 6 cm by 6 cm, is both compact and portable. For comparison, an ECG device was employed to collect synchronized ECG data.

As part of our analysis of VCG waveforms, we ensured a stable sleep posture and positioned the radar antenna beam to directly face the human thorax. This setup minimizes environmental interferences, allowing us to explore the common characteristics of VCG waveforms. Moreover, synchronously collecting radar and ECG signals is crucial for investigating the potential relationship between VCG waveforms and ECG, thereby providing physiological significance to the VCG waveforms.

Ten adults (six males and four females; mean age: 38.3±20.3; mean BMI: 22.5±3.24) participated in this study. The detailed information of all the subjects is listed in Table 1. The participating volunteers ranged in age from 21 to 76 years, with a balanced gender distribution and a wide range of BMI values. For each volunteer, 10 min of synchronized radar and ECG data were collected in the scene depicted in Figure 5(a). The subjects provided written informed consent before inclusion. This study was approved by Ethics Committee of Ruijin Hospital affiliated to Shanghai Jiao Tong University School of Medicine (EC REFERENCE No. (2024) Linlunshen No. 220).

4.3 Individual cardiac morphology analysis

Figure 5(b) shows a 15-s segment of data from subject 3. In this figure, panel I displays the synchronously collected ECG signals, panel II presents the segmented auxiliary signals with velocity feature enhancement processed by (17) based on the proposed segmentation method, panel III shows the VCG obtained using the proposed VAD-Wiener linear velocity cardiogram extraction method, and panel IV presents the DCG signal extracted using the PRF

Table 1 Information of subject.

Subject	Gender	Age (year)	BMI
1	Male	26	25.5
2	Male	24	19
3	Male	27	20.1
4	Male	29	18.6
5	Female	21	19
6	Female	25	23
7	Female	30	22
8	Male	61	26
9	Female	64	25
10	Male	76	27

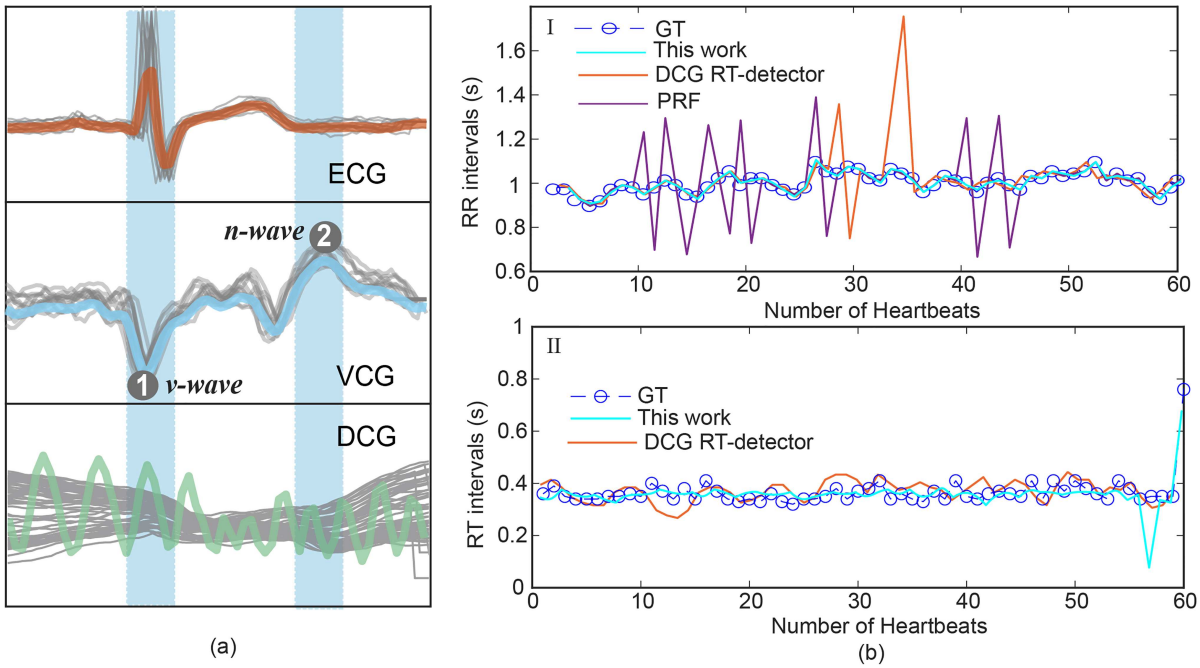

Figure 6 (Color online) (a) Morphology analysis of measured ECG, VCG and DCG; (b) comparison between the heart rhythms retrieved from the ECG and extracted VCG.

method. It can be seen that the enhanced segmented auxiliary signals in panel II, processed by (17), effectively exhibit two significant cardiac mechanical activities, marked by gray and green vertical dashed lines in Figure 5(b). These two activities have opposite velocity directions, corresponding to the peak velocity moments of cardiac contraction and relaxation, respectively. Comparing with the synchronously collected ECG signals, these two moments correspond to the R peak and the end of the T wave in the ECG, which, according to electrocardiography physiology, represent the onset of cardiac contraction and relaxation, respectively.

Figure 6(a) demonstrates the beat-by-beat heartbeats obtained using the segmented auxiliary signals of Figure 5(b). After extracting the VCG from radar echo data using the proposed methodology, the VCG signal is segmented into N cardiac cycles ($\mathrm{VCG}_{\mathrm{seg}}$) via the automatic cardiac beat segmentation algorithm described in Subsection 3.4. Each $\mathrm{VCG}_{\mathrm{seg}}$ segment is zero-padded to a uniform length M, and ensemble averaging is subsequently performed. The average cardiogram is derived as follows:

$$\mathrm{VCG}_{\mathrm{average}} = \frac{\sum_{i=1}^{N} \mathrm{VCG}_{\mathrm{seg}}}{N}. \tag{18}$$

Similar procedures were applied to generate the ECG and DCG waveforms shown in Figure 6(a). It can be observed that both ECG and VCG exhibit stable average waveforms, whereas the average DCG appears disorganized. This phenomenon indicates the steady-state characteristics of the VCG, making it more suitable for characteristic studies as a generic radar cardiogram waveform across a broad population compared to DCG. Additionally, based on the correspondence between VCG and ECG, the two distinctive morphological and physiological characteristic

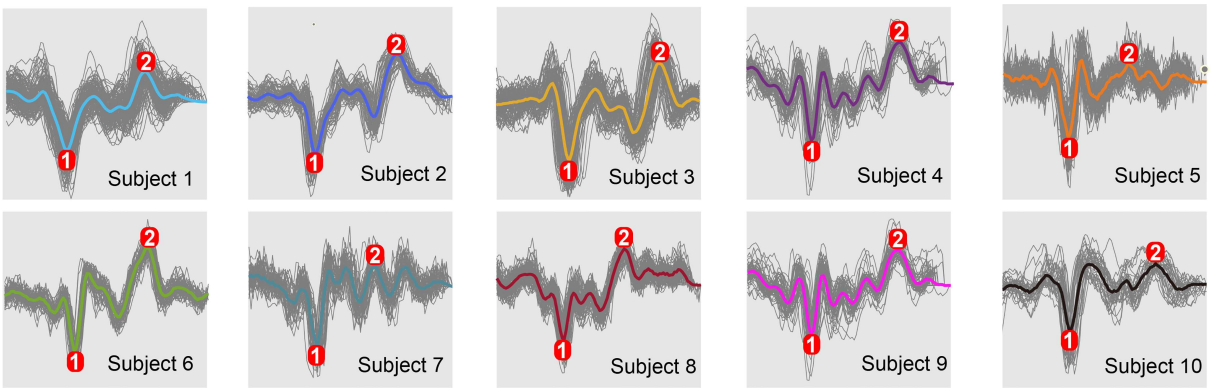

Figure 7 (Color online) Two-minute beat-by-beat VCG waveforms from 10 volunteers, with colored curves in the figure representing the average VCG waveforms of different subjects.

waveforms are named v-wave and n-wave, respectively, and are marked on the average VCG waveform in Figure 6(a). The names v-wave and n-wave are derived from their resemblance to the letters 'v' and 'n', respectively; the v-wave has a sharper shape, while the n-wave is smoother with a preceding notch.

To verify the accuracy of the proposed VAD-Wiener method for linear velocity cardiogram extraction, we processed a one-minute segment of data from subject 3. Based on the VCG signals obtained using our method, we extracted the cardiac RR intervals and RT intervals and compared them with the gold standard ECG, as shown in Figure 6(b). We also compared our method with previous cardiogram extraction methods PRF method and DCG RT-detector method. It can be seen that the accuracy of the RR interval extraction using our method significantly surpasses that of the PRF and DCG RT-detector methods. Additionally, since the PRF method cannot extract the cardiographic features corresponding to the T wave, we only compared the RT interval extraction performance with the DCG RT-detector method. It can be seen that our method demonstrates high accuracy. However, due to the relatively indistinct characteristics of the n-wave compared to the v-wave, there is a higher likelihood of inaccurate localization, as indicated by an outlier around the horizontal coordinate of 58 in the figure.

4.4 Reliability validation

Figure 7 shows the two-minute beat-by-beat VCG waveforms of 10 volunteers. It can be observed that the average waveforms of these 10 subjects exhibit various shapes, but still maintain a certain degree of morphological similarity. For example, the 1st v-wave marked with a red dot is clearly visible in the VCG waveforms of all 10 subjects. However, for the 2nd n-wave marked with a red dot, different individuals exhibit different waveform characteristics. This n-wave is relatively noticeable in most subjects, showing a more gentle peak compared to the v-wave. In subjects 5 and 7, the basic morphology of the n-wave has undergone some changes, but it still retains the physiological characteristic of the maximum point of positive velocity. Each individual has unique and distinctive physiological characteristics, and no two individuals have identical cardiac activities. This fundamental principle is reflected in the relatively broad population data set shown in Figure 7. Utilizing this characteristic, it is possible to achieve biometric identification based on VCG.

To further deepen the analysis of VCG waveform morphology and explore whether the VCG obtained under the standardized VCG detection and extraction process proposed in this paper has considerable consistency, the aforementioned describes that physiological signals exhibit stochastic stationary signal characteristics over a continuous period. Therefore, based on human physiology, beat-by-beat VCG signals collected over continuous periods should exhibit a certain degree of similarity. Thus, we use the average VCG waveforms of each subject's two-minute data shown in Figure 7 as templates, and investigate the Pearson correlation coefficient between the average waveforms of different numbers of continuous beats and the templates. The calculation method is as follows:

$$\rho = \frac{\mathrm{cov}(\frac{\sum_{i=1}^{n} \mathrm{heartbeats}(i,t)}{n}, \mathrm{template})}{\sigma \sigma_{\mathrm{template}}}, \tag{19}$$

$$\mathrm{template} = \frac{\sum_{i=1}^{N} \mathrm{heartbeats}(i,t)}{N}, \tag{20}$$

where template represents the subject's two-minute VCG template signal, N is the number of heartbeats within two minutes, and $\mathrm{heartbeats}(i,t)$ is the time-domain waveform of the VCG within the ith heartbeat cycle, cov

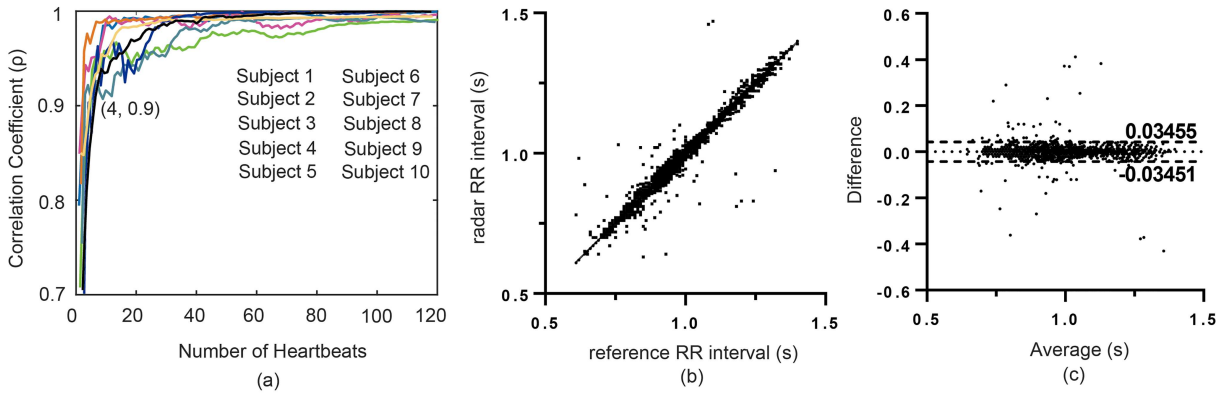

Figure 8 (Color online) (a) Convergence of the correlation coefficient between the cumulatively averaged VCG heartbeat and template VCG heartbeat with respect to number of heartbeats in the cumulative average for 10 subjects; (b) the correlation scatters plot of the RR intervals obtained by the proposed radar-based method and simultaneously recorded ECG device; (c) the Bland-Altman diagram of the RR intervals obtained by the proposed method and simultaneously recorded ECG device. The horizontal dotted line indicates the mean bias, and the dotted lines represent the upper and lower limits of the 95% confidence interval.

denotes the covariance operation, while σ denotes the standard deviation operation. The curves showing the change in Pearson correlation coefficients between the VCG waveforms of the 10 subjects and their individual templates as the number of included heartbeats increases is presented in Figure 8.

As seen in Figure 8(a), from the first heartbeat cycle, all subjects' VCG waveforms already have a correlation coefficient greater than 0.7 with the template signal. The curves of subjects 1 and 8 initially exhibited very high correlation (approximately 0.9). As the number of heartbeat cycles increased, most subjects' correlation curves displayed steady-state characteristics, showing increasing similarity to the template signal. After the fourth heartbeat cycle, all subjects exhibited a correlation coefficient greater than 0.9. The curve of subject 1 showed fluctuations between the 40th and 60th heartbeat cycles, but the overall correlation coefficient during this period remained above 0.95. This indicates that while the overall VCG waveform characteristics maintain a certain consistency, there are also inherent differences and variations between individual heartbeats, resulting in some fluctuations. This phenomenon aligns with the physiological characteristic of heart rate variability, which is that the intervals between heartbeats in a normal human are not completely identical, causing some rhythmic or activity-based differences.

As previously mentioned, to verify the accuracy of the standardized VCG detection method proposed in this paper, we can identify the v-wave and calculate the RR intervals, which can then be compared with the RR intervals extracted from the simultaneously collected ECG signals. Thus, we utilized the segmented auxiliary signals generated by the segmentation method proposed in Subsection 3.4 of this paper to enhance the v-wave effectively. Then, using the findpeaks method, we extracted the cardiac RR intervals and statistically compared them with the ground truth RR intervals extracted from the simultaneously collected gold-standard ECG signals.

Figure 8(b) shows the correlation analysis between the RR intervals extracted from the radar and the reference RR intervals extracted from the ECG. The figure presents the results of a simple linear regression on the scatter plot, with the best-fit line having a slope of 0.9876 and intercepts of -0.01231 and 0.01216 for the XY axes, respectively. The Pearson correlation coefficient between the radar RR intervals and the ECG RR intervals is 0.9854. These results demonstrate a strong correlation between the VCG extraction method proposed in this paper and the gold standard. Additionally, Figure 8(c) shows the Bland-Altman analysis results of the RR intervals. The mean difference between the values detected by the proposed method and the reference values is close to zero, and the 95% confidence intervals are all below 0.035 s.

Notably, as can be seen from the distribution of RR interval scatter plots in Figures 8(b) and (c), the 6123 heartbeat cycles of the 10 volunteers have a wide range of durations. This also demonstrates that the VAD-Wiener method proposed in this paper has excellent velocity cardiogram recovery characteristics across different heartbeat activity intervals.

4.5 VCG morphology analysis in different conditions

Based on the mechanism of radar detection of cardiac activity, what the radar actually detects are the micromovements on the surface of the chest cavity caused by the mechanical activity of the heart. In previous studies, all data were obtained using an experimental setup illustrated in Figure 5(a), employing a direct radar irradiation method on the chest to acquire VCG waveforms. In fact, the mechanical activity of the heart causes varying degrees of

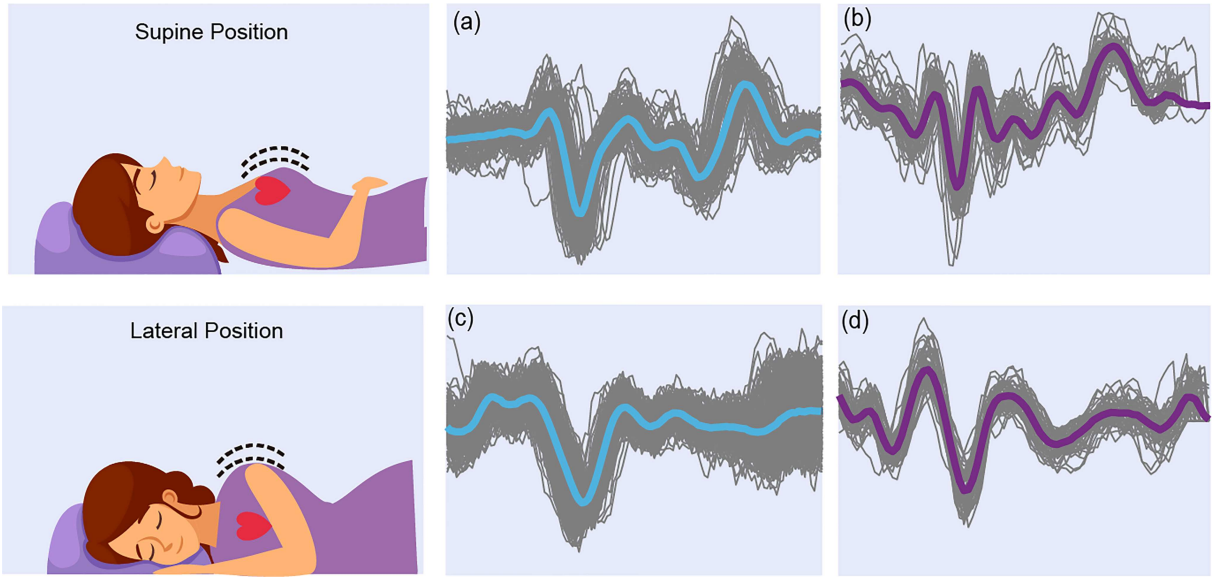

Figure 9 (Color online) The beat-by-beat VCG waveforms of subject 1 (a) in supine position, (c) in lateral position. The beat-by-beat VCG waveforms of subject 4 (b) in supine position, (d) in lateral position.

micromovements throughout the upper body. To further investigate how different radar irradiation positions affect the VCG waveforms and considering practical application scenarios, we conducted VCG collection experiments on subjects 1 and 4 in different postures.

The left of Figure 9 shows two experimental postures. One is the general posture used in previous studies, where the radar directly irradiates the surface of the chest, theoretically capturing significant micromovements caused by the heart. The other posture is lying on the side, where the radar irradiates the shoulder and back of the subject. Figures 9(a) and (c) display the two-minute VCG waveforms and average template signals extracted using the proposed VAD-Wiener method for subject 1 in these two postures. It can be observed that the n-wave disappears when lying on the side, likely because the micromovements induced by cardiac activity on the shoulder and back are too minimal, leading to greater signal loss through body tissue during transmission. However, due to the inherently strong kinematic characteristics of cardiac contraction, the v-wave remains clearly visible. Figures 9(b) and (d) show the two-minute VCG waveforms and average template signals extracted using the proposed VAD-Wiener method for subject 4 in these two postures. Similarly, significant changes in the VCG morphology are observed when lying on the side compared to lying flat. The n-wave is difficult to identify, and the detailed waveform of the overall template signal is greatly reduced. This is likely because the signals conducted to the lateral side are much weaker than those to the front of the thorax during cardiac mechanical activity. Nevertheless, the v-wave remains clearly visible.

We have also collected data from patients with abnormal cardiac conditions in a hospital setting. The experimental results obtained after processing with the method proposed in this paper are illustrated in Figure 10. As can be seen from the figure, the v-wave in the VCG waveform of the patient with atrial fibrillation is still clearly visible and retains its characteristic sharp waveform features. However, the n-wave is difficult to discern. Additionally, the T wave in the simultaneously acquired ECG waveform has also disappeared. This indicates that the waveform characteristics of the VCG signal maintain a certain degree of repeatability even in populations with cardiac abnormalities.

5 Discussion

In this study, we introduced a framework for the stable representation of cardiac mechanical activity using VCGs; the proposed VCG demonstrated considerably higher cardiogram waveform stability than the DCG. Based on the stochastic stationary properties of human physiological signals, we proposed an accurate linear extraction method, the VAD-Wiener algorithm. The VCG framework proposed in this study lays the foundation for subsequent extensive analysis of VCG waveforms across diverse populations. For comparison, we provide Table 2 [7,12,13,18,29], which summarizes previous and recent studies on radar cardiogram detection.

Additionally, we investigated the extraction of common characteristic waveforms from cardiograms obtained from

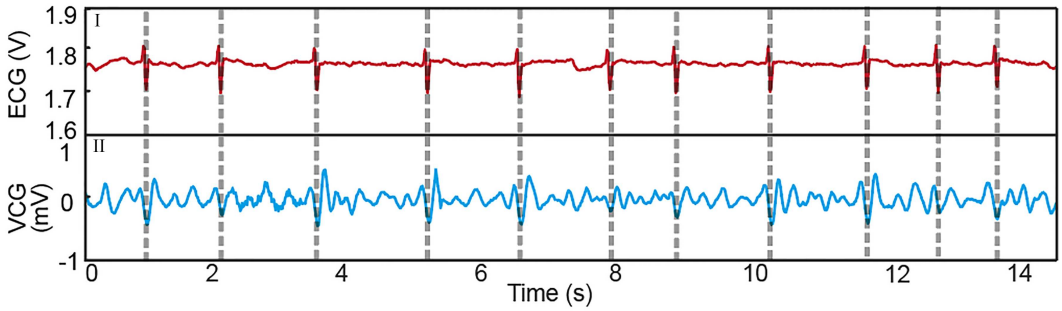

Figure 10 (Color online) VCG waveform analysis for a patient with atrial fibrillation.

Table 2 Comparison with other radar-based cardiogram detection studies.

Work	Data size	Radar working mode and frequency	Processing method	Cardiogram detected	RRI accuracy	Waveform analysis
[12]	10 h of 35 subjects (between the ages of 18 and 65)	FMCW, 77 G	Deep learning	Quasi-ECG	Median error: 14 ms	Y
[13]	12 subjects (aged between 22 and 39)	FMCW, 120 G	Adaptive template matching	DCG	BA 95% confidence: 43.9 ms	N
[29]	6222 subjects	FMCW, 60 G	VMD and harmonics analysis	–	Median RMSSD error: 53.8 ms	N
[7]	10 mins of 3 subjects	CW, 24 G	Parameterized respiratory filter	DCG	RMSE: 10.84 ms	Y
[18]	100 s of 5 subjects	CW, 24 G	DCG-RT detector	DCG	NRMSE: 2.03%	N
This work	6123 heart cycles of 10 subjects (aged between 21 and 76 years and BMI between 18.6 and 27)	CW, 24 G	VAD-wiener	VCG	BA 95% confidence: 34.5 ms	Y

different individuals and the physiological significance of these waveforms. Despite their differences, commonly used cardiograms describing cardiac activity, such as ECG, BCG, and SCG, exhibit similar waveform characteristics across different individuals. Therefore, for VCGs, which directly describe the mechanical activity of the heart, there should be corresponding VCG characteristic waveforms representing typical contraction and relaxation activities of the heart. Consequently, we employed a broad dataset of volunteers encompassing a wide range of ages and body types. Using the proposed framework, we verified that the VCG waveforms obtained from different individuals exhibit common v- and n-wave characteristics, corresponding to the maximum cardiac contraction and relaxation velocities, respectively. By comparing these characteristic waveforms with simultaneously collected ECG signals, we validated the accuracy of the proposed method.

However, during the course of this work, we found that the n-wave characteristic waveform could not be well detected in some populations; therefore, further investigation is required. In contrast, the v-wave waveform consistently demonstrated clear recognizability under various conditions and detection methods, making the accurate contactless detection of cardiac RR intervals possible.

For different radar irradiation positions on the same individual, the obtained VCG waveforms may be inconsistent. This implies that in potential future applications, such as biometric identification, VCG would likely require highly stringent detection conditions.

In future work, based on the VCG detection framework proposed in this study, extensive and large-scale datasets can be established. These datasets can be used for the classification of heart diseases. By integrating AI algorithms, meaningful disease prediction based on VCGs can be achieved.

Acknowledgements This work was supported in part by National Key R&D Program of China (Grant No. 2022ZD0160704), National Natural Science Foundation of China (Grant Nos. 62188102, 62171277), and Shanghai Jiao Tong University Medical-Engineering Interdisciplinary Research Fund (Grant No. YG2023QNA30). We are also grateful for the support provided by Shanghai Artificial Intelligence Laboratory and Hecaray Technologies throughout this study.

References

1 Gutta S, Cheng Q. Joint feature extraction and classifier design for ECG-based biometric recognition. IEEE J Biomed Health Inform, 2016, 20: 460–468
2 Wiens A D, Etemadi M, Roy S, et al. Toward continuous, noninvasive assessment of ventricular function and hemodynamics: wearable ballistocardiography. IEEE J Biomed Health Inform, 2015, 19: 1435–1442
3 Inan O T, Migeotte P F, Park K S, et al. Ballistocardiography and seismocardiography: a review of recent advances. IEEE J Biomed Health Inform, 2015, 19: 1414–1427

4 Shandhi M M H, Semiz B, Hersek S, et al. Performance analysis of gyroscope and accelerometer sensors for seismocardiography-based wearable pre-ejection period estimation. IEEE J Biomed Health Inform, 2019, 23: 2365–2374
5 Huang Y, Wang Y X, Zhou X, et al. Interference mitigation and target detection for automotive FMCW radar with range-Doppler sparse regularization. Sci China Inf Sci, 2024, 67: 199303
6 Dong S, Zhang Y, Ma C, et al. Doppler cardiogram: a remote detection of human heart activities. IEEE Trans Microwave Theor Techn, 2020, 68: 1132–1141
7 Dong S, Li Y, Lu J, et al. Accurate detection of Doppler cardiograms with a parameterized respiratory filter technique using a K-band radar sensor. IEEE Trans Microwave Theor Techn, 2023, 71: 71–82
8 Li C Z, Ling J, Li J, et al. Accurate Doppler radar noncontact vital sign detection using the RELAX algorithm. IEEE Trans Instrum Meas, 2010, 59: 687–695
9 Wang J, Wang X, Chen L, et al. Noncontact distance and amplitude-independent vibration measurement based on an extended DACM algorithm. IEEE Trans Instrum Meas, 2014, 63: 145–153
10 Fan T, Ma C, Gu Z, et al. Wireless hand gesture recognition based on continuous-wave Doppler radar sensors. IEEE Trans Microwave Theor Techn, 2016, 64: 4012–4020
11 Xu W, Li Y, Gu C, et al. Large displacement motion interferometry with modified differentiate and cross-multiply technique. IEEE Trans Microwave Theor Techn, 2021, 69: 4879–4890
12 Chen J, Zhang D, Wu Z, et al. Contactless electrocardiogram monitoring with millimeter wave radar. IEEE Trans Mobile Comput, 2024, 23: 270–285
13 Yang Z, Yang H, Hu A, et al. An adaptive template matching method for noncontact cardiac inter-beat interval detection using a 120 GHz FMCW radar. IEEE Trans Instrum Meas, 2025, 74: 1–12
14 Li M, Lin J. Wavelet-transform-based data-length-variation technique for fast heart rate detection using 5.8-GHz CW Doppler radar. IEEE Trans Microwave Theor Techn, 2018, 66: 568–576
15 Dong S, Gu C, Mao J. Contactless cardiac RR intervals estimation in radar-based cardiogram detection. In: Proceedings of the 56th Asilomar Conference on Signals, Systems, and Computers, 2022. 1137–1141
16 Qu L, Liu C, Yang T, et al. Vital sign detection of FMCW radar based on improved adaptive parameter variational mode decomposition. IEEE Sens J, 2023, 23: 25048–25060
17 Ding C, Yan J, Zhang L, et al. Noncontact multiple targets vital sign detection based on VMD algorithm. In: Proceedings of the IEEE Radar Conference (RadarConf), 2017. 727–730
18 Dong S, Li Y, Gu C, et al. Robust cardiac timing detection technique with vectors analytic demodulation in Doppler cardiogram sensing. IEEE Trans Microwave Theor Techn, 2024, 72: 4866–4877
19 Zhang J, Wu Y, Chen Y, et al. Health-radio: towards contactless myocardial infarction detection using radio signals. IEEE Trans Mobile Comput, 2020, 21: 585–597
20 Pollack G H. Maximum velocity as an index of contractility in cardiac muscle. Circ Res, 1970, 26: 111–127
21 Swynghedauw B. Molecular mechanisms of myocardial remodeling. Physiol Rev, 1999, 79: 215–262
22 Kiriazi J, Lubecke O, Lubecke V. Radar cross section of human cardiopulmonary activity for recumbent subject. In: Proceedings of the Annual International Conference of the IEEE Engineering in Medicine and Biology Society, 2009. 4808–4811
23 Italian National Research Council, Institute for Applied Physics. An Internet resource for the calculation of the dielectric properties of body tissues in the frequency range 10 Hz–100 GHz. http://niremf.ifac.cnr.it/tissprop/
24 Nguyen D, Yamada S, Park B. Noise considerations for remote detection of life signs with microwave Doppler radar. In: Proceedings of the 29th Annual International Conference of the IEEE Engineering in Medicine and Biology Society, 2007. 1667–1670
25 Salamin Y, Pan J, Wang Z, et al. Eliminating the impacts of flicker noise and DC offset in zero-if architecture pulse compression radars. IEEE Trans Microwave Theor Techn, 2014, 62: 879–888
26 Droitcour A D, Boric-Lubecke O, Kovacs G T A. Signal-to-noise ratio in Doppler radar system for heart and respiratory rate measurements. IEEE Trans Microwave Theor Techn, 2009, 57: 2498–2507
27 Gu C, Wang G, Inoue T, et al. Doppler radar vital sign detection with random body movement cancellation based on adaptive phase compensation. In: Proceedings of EEE MTT-S International Microwave Symposium Digest, 2013. 1–3
28 McLane I, Lauwers E, Stas T, et al. Comprehensive analysis system for automated respiratory cycle segmentation and crackle peak detection. IEEE J Biomed Health Inform, 2021, 26: 1847–1860
29 Ni H, Wang Y, Yao K, et al. Cyclical palmitoylation regulates TLR9 signalling and systemic autoimmunity in mice. Nat Commun, 2024, 15: 1